PAPER

Check for updates

Tuning the stability of a model quasicrystal and its approximants with a periodic substrate

Nydia Roxana Varela-Rosales [ID] and Michael Engel [ID] *

Quasicrystals and their periodic approximants are complex crystalline phases. They have now been observed in many metallic alloys, soft matter systems, and particle simulations. In recent experiments of thin-film perovskites on solid substrates, the type of complex phase was found to change depending on thermodynamic conditions and the type of substrate used. Here, we investigate the effect of a substrate on the relative thermodynamic stability of a two-dimensional model quasicrystal and its approximants. Our simulation model is particles interacting *via* the Lennard-Jones–Gauss potential. Our numerical methods are molecular dynamics simulations and free energy calculations that take into account phason flips explicitly. For substrates interacting weakly with the particles, we observe an incommensurate–commensurate transition, in which a continuous series of quasicrystal approximants locks into a small number of approximants. Interestingly, we observe that the 3/2 approximant exhibits phason mode fluctuations in thermodynamic equilibrium. Such fluctuations are reminiscent of random tiling and a phenomenon usually associated only with quasiperiodic order. For stronger substrates, we find an enhancement of the stability of the dodecagonal quasicrystal and variants of square lattices. We explain all observed phenomena by the interplay of the model system with the substrate. Our results demonstrate that designing novel complex periodic and quasiperiodic structures by choice of suitable substrates is a promising strategy.

1 Introduction

The discovery of structures with point group symmetries forbidden in periodic crystals[1] created a new field of crystallography, the field of quasicrystals[2,3] (QCs). Bulk, three-dimensional QCs became popular as candidates for materials with functional properties such as thermal insulators,[4] coating materials,[5,6] photonic crystals[7] and superconductors.[8] The first atomic QC in two dimensions was found only recently in the thin-film perovskite $BaTiO_3$ on a Pt substrate.[9] This discovery inspired follow-up work on thin-film perovskite QCs as well as their approximants at different chemical compositions.[10–15] Despite significant efforts, how these perovskite QCs form and why they are stable remain mostly open questions. Answering these questions is of interest to simulation studies but is difficult to address with quantum mechanical methods at the atomic scale because the lack of periodicity and slow phason relaxation in QCs require large systems over long simulation times.[16,17] Coarse-grained model systems are advantageous because they capture the essential physics and offer a route towards elucidating the relative thermodynamic stability of the involved phases and their phase transformation pathways.

Institute for Multiscale Simulation, Friedrich-Alexander-Universität Erlangen-Nürnberg, 91058 Erlangen, Germany. E-mail: michael.engel@fau.de

Two-dimensional particle systems in the presence of a substrate exhibit intricate structure formation phenomena caused by the competition of two length scales. These length scales are the size of the unit cell of the unperturbed particle system and the periodicity of the substrate. The competition of the length scales can introduce novel commensurate and incommensurate phases.[18,19] Incommensurability also plays a role in nanotribology by influencing Aubry transitions in systems of colloids sliding on a substrate.[20–23] Three factors are relevant for controlling the phase behavior in such systems: substrate potential depth, substrate periodicity, and the crystallographic symmetries of the particle system and the substrate.[24]

The investigation of thin QC films on a substrate can be divided into two classes of systems. The first class comprises systems, which are templated to have QC order using a QC substrate. Such QC films have been realized at the nanoscale as atomic adlayers.[25–28] And at the colloidal scale, QC laser fields can be finely tuned to induce a gradual transition from an unperturbed system to a frozen QC.[29–33] The second class comprises systems with intrinsic QC order. That is, such systems are QCs even in the absence of the substrate. It is suspected that thin film perovskite QCs fall into the latter class.[9] Both classes of systems can show interesting phase behavior as the substrate is tuned.

There exist many simulation models for two-dimensional QCs. Prominent examples are binary mixtures of particles that

interact with the Lennard-Jones potential,[34,35] one-component systems of particles with interaction potential minima on two length scales,[36–38] and anisotropic particles with patchy interactions.[39,40] Here, we study the Lennard-Jones–Gauss (LJG) potential, which stabilizes a number of one-component QCs and approximants already in the absence of a substrate.[37,41] We use this coarse-grained model to investigate the possibility of targeting specific approximants by tuning substrate parameters. As we will see, the LJG system can behave like a thin film QC in both the first and the second classes, depending on the choice of thermodynamic conditions and the substrate.

2 Methods

2.1 Coarse-grained model

As in our previous work,[41] we investigate a coarse-grained two-dimensional model system, which is known to form different types of periodic and quasiperiodic phases.[37] In this model, identical particles interact isotropically with the LJG potential given by

$$V_{LJG}(r) = \frac{1}{r^{12}} - \frac{2}{r^6} - \varepsilon_{LJG} \exp\left(\frac{-(r - r_{LJG})^2}{2\sigma_{LJG}^2}\right). \quad (1)$$

The potential parameters are fixed in this work at $\varepsilon_{LJG} = 1.8$, $r_{LJG} = 1.42$, and $\sigma_{LJG}^2 = 0.042$ to stabilize a dodecagonal QC at intermediate temperatures.[41] The phase diagram of the LJG potential at these parameters contains a number of phases described by tilings made from squares, triangles, and pentagons. The sequence of phases can be described according to the underlying symmetry change[41]

$$p3m1 \xrightarrow{0.24} p6m \xrightarrow{0.35} p12m \xrightarrow{0.36} p4m \xrightarrow{0.41} E(2), \quad (2)$$

where the symbols are the wallpaper groups of the phases and the numbers above the arrows indicate the critical temperature of the phase transitions. It has been shown that a relatively simple periodic approximant (wallpaper group $p3m1$) is the energetic ground state stable at $T = 0$. This simple approximant transitions via a series of increasingly more complex hexagonal approximants (wallpaper group $p6m$) continuously to a dodecagonal QC (wallpaper group $p12m$) in the temperature range $0.24 < T < 0.35$. Towards a slightly higher temperature, at $T = 0.36$, the QC converts into a square tiling (wallpaper group $p4m$) before melting at $T = 0.41$ into the liquid. The liquid has no broken rotational or translational symmetry and is thus represented by the group of all isometries, the Euclidean group $E(2)$.

The phase behavior of the LJG system is only known in the absence of a substrate. Here, we add a substrate by including an external potential. We mimic the effect of the Pt (111) substrate for thin-film perovskite QCs by choosing an external potential in the form of a hexagonal lattice by superposition of three plane waves,

$$V_{ext} = \varepsilon \frac{\varepsilon_{LJG}}{T} \sum_{j=0}^{2} \frac{\cos(2\pi k_j \cdot r/\lambda)/3 + 1}{2} \quad (3)$$
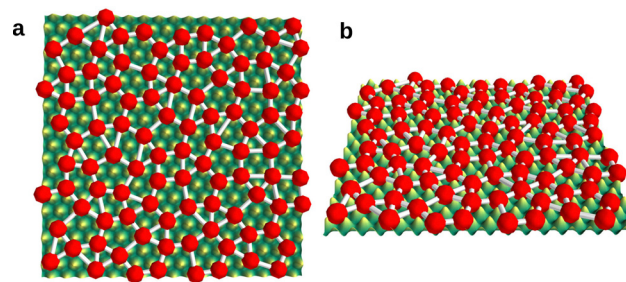

Fig. 1 Schematic depiction of the model system of this work. Particles (red) interacting with themselves via the LJG potential and with an external potential simulating the substrate (green/yellow). The particles form a dodecagonal quasicrystal. Bonds (gray) connect nearest neighbors and form three types of tiles: triangles, squares, and pentagons. Tiles are deformed due to the vibrational motion of the particles at an elevated temperature. (a) Top view. (b) Side view at an angled perspective.

with $k_j = (\cos(\pi j/3), \sin(\pi j/3))$. There are two parameters, substrate potential depth ε and substrate periodicity λ. A prefactor of ε_{LJG}/T is included for convenience to ensure that the region of interest is approximately rectangular in the T–ε parameter plane (see assembly diagram below, Fig. 5). A schematic depiction of the model, comprising of the particles (red) interacting with themselves and the periodic substrate (green/yellow), is shown in Fig. 1.

To justify the choice of a model system for this work, we need to discuss phason modes. Phason modes are dynamic modes characteristic of QCs. They are realized as a collective rearrangement of finite clusters of tiles and can be decomposed into a series of elementary particle displacements called phason flips. In many common QCs, like for example, the Penrose tiling, phason mode excitation requires only a low activation energy and can occur locally with only a small number of phason flips. We call phason modes such as those found in the Penrose tiling continuously excitable. In other QCs, for example the square-triangle tiling, phason mode excitation requires creating a pair of defects and propagating each defect along a path rearranging the tiling in the process until the defects annihilate. In the square-triangle tiling, this process is called a zipper.[42] Zippers are not efficient in relaxing the square triangle-tiling. We call phason modes such as those found in the square-triangle tiling therefore not continuously excitable. Continuously excitable phason modes are found in thin-film perovskite QCs where they involve rhomb tiles with small interior angle $30°$. Because of the presence of continuously excitable phason modes, perovskite QCs can efficiently relax their tiling and transform to and from approximants.[10,11] We chose to study the LJG model system because it stabilizes and includes continuously excitable phason modes in the $p6m$ and $p12m$ phases.[41] This means that our model system is similar to perovskite QCs in the character of its phason flips and the phase transformations between approximants and the QC.

2.2 Tiling construction in hyperspace

The tilings of the dodecagonal QC and its approximants in the LJG model system can be described by the cut-and-project

method[43,44] in a four-dimensional hyperspace. We construct tiling models in two steps.

In the first construction step, approximants of the quasi-crystalline shield tiling[45] are constructed. The projection matrices on the two-dimensional physical (or parallel) space are

$$\boldsymbol{P}^{\parallel} = \frac{1}{\sqrt{2}} \begin{bmatrix} c_0 & c_1 & c_2 & c_3 \\ s_0 & s_1 & s_2 & s_3 \end{bmatrix} \tag{4}$$

with $c_i = \cos((i + 1/2)\pi/6)$ and $s_i = \sin((i + 1/2)\pi/6)$. The projection matrix on the two-dimensional internal (perpendicular) space is

$$\boldsymbol{P}^{\perp} = \frac{1}{\sqrt{2}} \begin{bmatrix} c'_0 & c'_5 & c'_{10} & c'_3 \\ s'_0 & s'_5 & s'_{10} & s'_3 \end{bmatrix} \tag{5}$$

with $c'_i = \cos(i\pi/6 + \phi)$ and $s'_i = \sin(i\pi/6 + \phi)$. The occupation domain for the shield tiling is a dodecagon with twelve vertices $v_i = (c'_i, s'_i)$, $i = 1,\ldots,12$. The parameter

$$\phi = \arctan\left(\frac{t - \sqrt{3}}{t + \sqrt{3}}\right) \quad \text{with} \quad t = 2\frac{q}{p} - 1 \tag{6}$$

constructs the dodecagonal shield tiling for $\phi = 0$ and q/p periodic approximants for $\phi \neq 0$. In this notation, approximants are labeled by two integers, q and p. Their ratio ranges from $q/p = 2$ for the simple periodic approximant with wallpaper group $p3m1$ to $q/p = (\sqrt{3} + 1)/2$ for the quasicrystal with wallpaper group $p12m$. This means that the simple periodic approximant is identified as a 2/1 approximant. All approximants with wallpaper group $p6m$ can be constructed in the range $(\sqrt{3} + 1)/2 < q/p < 2$. The approximants have rectangular unit cells with lattice constants $b_x = b_y\sqrt{3}$ and $b_y = (t + \sqrt{3})p/\sqrt{2}$. The approximants of the shield tiling constructed so far are built from three basic tiles: square, triangle, and shield.[45]

In a second construction step, the basic tiles square, triangle, and shield are decorated by placing one particle in the center of the square tiles, one particle in the center of the triangle tiles, and three particles as a regular triangle in the center of the shield tiles. The result is the tilings of interest, built from three larger tile types: square, triangle, and slightly deformed pentagon. Examples of these resultant tilings are found in Fig. 1 and Fig. 6. The combination of these tile decorations forms a substitution rule.

2.3 Simulations and free energy calculations

We perform simulations and free energy calculations using a combination of molecular dynamics (MD) and Monte Carlo (MC) to accelerate relaxation and exploration of phase space. MD is used to sample phonon modes and configurational entropy. MC is used to sample phason modes.[46] From the van Hove autocorrelation function,[38] we observe that all phason flips readily occur over a single flip distance near $r = 1$ and that most particles can perform phason flips. This demonstrates that phason modes are continuously excitable *via* local phason

flips and do not require significant activation energy. We use the HOOMD-blue molecular dynamics simulation package[47,48] as the basis for our simulations and further extend it to include MC moves. For MD, the integration timestep is 0.01. The NVT ensemble with Nosé–Hoover thermostat is used and open boundary conditions are applied. The Boltzmann constant is set to 1. For MC, we attempt a phason flip in MC by choosing a particle at random and a flip vector uniformly distributed in the ring $0.9 < r < 1.1$. The MC move is accepted according to the Metropolis acceptance criterion. The measured acceptance rate of MC phason flips is about 10%. Periodic boundary conditions are employed to minimize finite size effects. We now discuss the two different simulation modes used in this work.

In the first simulation mode, used for generating a diagram summarizing assembly behavior as a function of model parameters, called an assembly diagram, and for studying phase transitions, we perform MD simulations without MC moves. We simulate 10 000 particles in a quadratic simulation box of a box edge length 300. The particles are initially placed in a central circle with a number density of 0.3. The particles crystallize over time into a roughly circular, compact cluster, which corresponds to a solid–gas coexistence. We chose this setup to effectively obtain open boundaries for the crystalline cluster. Such open boundaries are essential for efficient phason relaxation because phason relaxations are generally suppressed by the topological constraints of periodic boundary conditions.

In the second simulation mode, used for the calculation of Helmholtz free energies, we combine MD and MC. 5000 MD sweeps, *i.e.*, moving each particle 5000 times, are alternated with 5000 MC steps, *i.e.*, attempting to perform a phason flip for 5000 randomly chosen particles. System size varies for different approximants and the QC between 4000 and 12 000 particles. In contrast to the first simulation mode, the simulation box for approximants is now completely filled to prevent solid–gas coexistence and to avoid phase transitions between approximants. For the QC, we simulate with open boundaries and only consider particles sufficiently fare from the surface. We first relax constructed approximants in an NPT simulation and then perform free energy integration in the NVT ensemble. In this way, the number density of simulations in the second simulation mode is guaranteed to agree with that of simulations in the first simulation mode.

We use the Frenkel–Ladd (FL) method[49] to compute free energies. FL performs a thermodynamic integration over a parameter λ. It interpolates between the system of interest at $\lambda = 0$ and an Einstein crystal at $\lambda = 1$. In an Einstein crystal, each particle is connected to a reference position by a harmonic spring. The integration is performed as

$$F = F_{\text{Ein}} - \int_0^1 \Delta F(\lambda)\mathrm{d}\lambda, \tag{7}$$

where ΔF is measured from simulation. Because the reference free energy of the Einstein crystal, F_{Ein}, is known, we can calculate in this way absolute free energies.

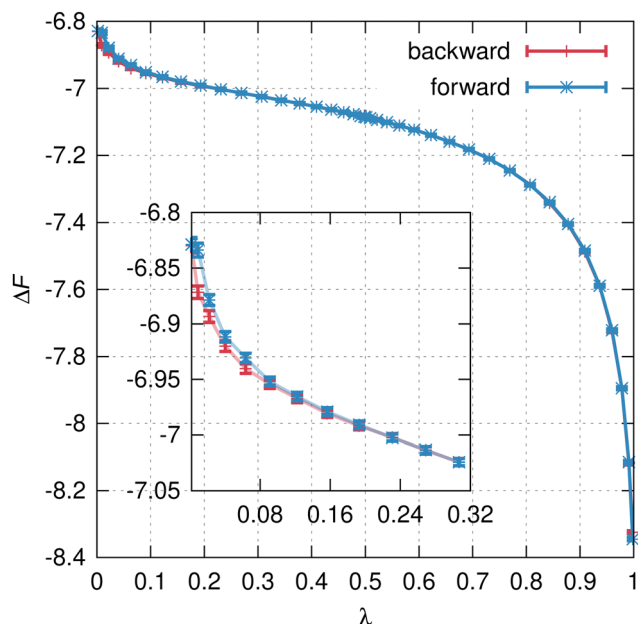It is important to check that the system remains in equilibrium throughout the FL integration. We perform such a check

Fig. 2 Frenkel–Ladd integration for the 2/1 approximant at $T = 0.25$. We measure the integrand ΔF in simulation by time-averaging at each λ point in both forward direction and backward direction. The inset shows a zoom-in to small λ values.

by calculating the free energy in the forward direction (increasing λ) and in the backward direction (decreasing λ) and by checking for hysteresis. The absence of hysteresis is an indication that the free energy calculation is accurate. A test FL integration for the 2/1 approximant is shown in Fig. 2. Forward and backward curves for ΔF agree, except for a small difference near $\lambda = 0$. At small λ, particles diffuse strongly through the system, which slows down equilibration. We use our test FL integration to adjust the numerical parameter to ensure that the hysteresis is sufficiently small. For numerical integration in production calculations, we use Legendre–Gauss quadrature with 20 λ points. Each λ point is simulated for $25\,000$ MD sweeps. The spring constant of the Einstein crystal is $\Lambda_E = 100$. This value guarantees similar vibrational dynamics in the Einstein crystal and the system of interest as indicated by an approximately flat integrand.[50]

We validate the FL implementation by comparison to reported free energies[41] for the continuous transition $p3m1 \rightarrow p12m$ in the absence of a substrate at $\varepsilon = 0$. We calculate free energies $F_n(T)$ for six constructed approximants $q/p = n/10$ with $n \in [15,\dots,20]$ and a well-equilibrated QC. We follow the continuous transition from the 2/1 approximant to the quasicrystal via the superstructure wave vector[41]

$$q_s = \frac{8\pi}{\sqrt{6}} \frac{2p - q}{2q + (\sqrt{3} - 1)p}. \tag{8}$$

This wave vector is calculated from the distance between first-order satellite peaks and main diffraction peaks in reciprocal space.[41] The appearance of satellite peaks is a consequence of the presence of structural modulations in the
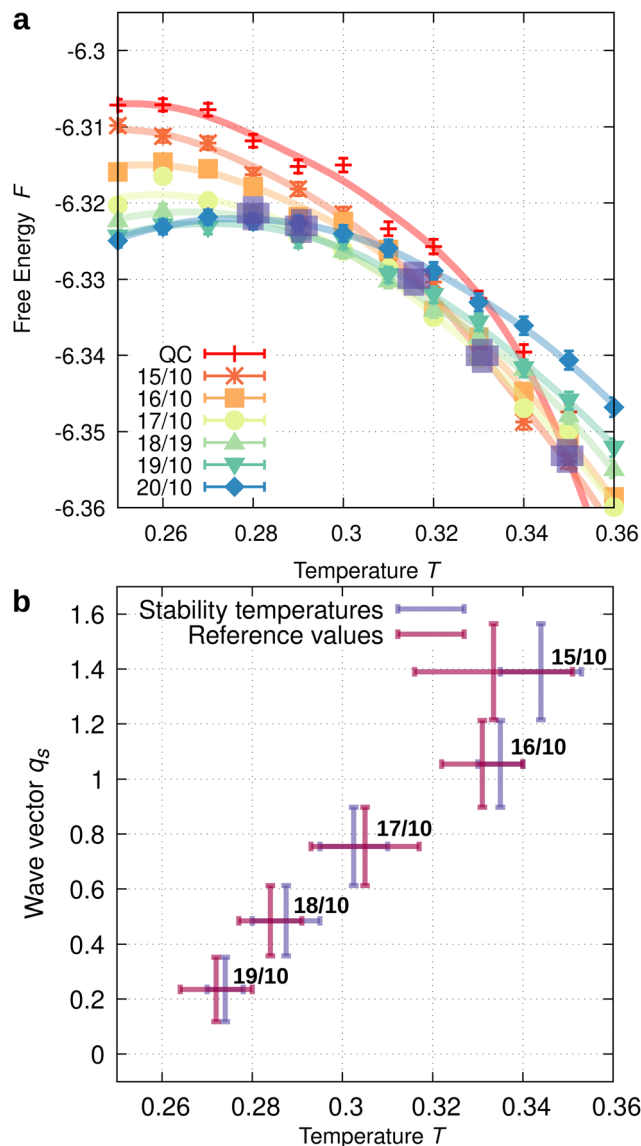

Fig. 3 (a) Helmholtz free energies $F_n(T)$ for a well-equilibrated quasicrystal and six approximants $n/10$, $n = 15,\dots,20$. Standard errors are estimated from eight independent FL calculations. Purple plus markers indicate the stability temperatures of approximants. Data shows the forward branch of the free energy calculation. (b) Validation of the free energy calculation with the FL plus phason model relaxation method. The superstructure vector grows linearly with temperature from the 2/1 approximant to the QC. Error bars on the temperature axis connect the FL calculation for the forward and the backward calculations. Stability temperatures for approximants agree with reference values[41] within the error bars.

approximants. We define the stability temperature of the approximant $n/10$ as the intersection of F_{n-1} and F_{n+1}. As an exception, instead of the 14/10 approximant, we use a well-equilibrated quasicrystal.

Our implementation of the FL plus phason mode relaxation algorithm shown in Fig. 3(a) accurately reproduces prior work.[41] In particular, we reproduce the reported linear increase of the wave vector q_s as a function of temperature (Fig. 3(b)). The agreement with prior work validates our free energy calculation with the FL plus phason model relaxation method.

3 Results

3.1 Molecular dynamics simulations

We analyze the crystallization behavior of our system by performing 77 MD simulations at seven temperatures $0.2 \leq T \leq 0.5$ in steps of 0.05 and for eleven substrate potential depths $0.0 \leq \varepsilon \leq 0.1$ in steps of 0.01. Substrate periodicity is fixed at $\lambda = 0.5$. This value is inspired by a direct comparison of relevant length scales in our simulations and the perovskite QCs on a Pt substrate.[11] Each simulation is run for 10^8 integration steps and the final simulation snapshot at the end of the run is analyzed. In this subsection, we first perform a general analysis of the orientational order and then conduct a more in-depth analysis of the observed structures by visual inspection and with the help of diffraction patterns.

3.1.1 Local orientational order analysis.

We quantify the presence of n-fold local orientational order via the Mermin order parameter[51] defined as

$$\Psi_n = \frac{1}{N} \sum_j \frac{1}{N_j} \sum_{k\,\mathrm{NN}_j} \exp(in\theta_{jk}), \tag{9}$$

where N is the number of particles, N_j is the number of nearest neighbors (NNs) of particle j using the cut-off $r = 2.5$, and θ_{jk} is the orientation of the nearest neighbor bond connecting particle j and particle k. The Mermin order parameters for $n = 6$ and $n = 4$ are also called the hexatic and quadratic order parameters, respectively. We are specifically interested in these order parameters because we expect to observe a competition between the quadratic order at high temperature T (as previously found in the LJG potential[41]) and the hexagonal order of the substrate.

The results of the local orientational order analysis are shown in Fig. 4. Indeed, there exists a competition between quadratic and hexagonal local orientational order. Hexagonal local order dominates at high T. Here the liquid phase is expected. In contrast, the quadratic local order dominates at intermediate T and high ε. Apparently, the substrate does not promote local hexagonal order but instead local quadratic order. This observation will be discussed further below. The gradual variation of local orientational order across the T–ε parameter plane indicates that the particles can react smoothly to changes in temperature and the substrate at a local level. We also observe that the presence of thermal fluctuations dominates over crystallographic symmetry in our two-dimensional system, smearing out the boundaries separating ordered phases. This precludes using the Mermin order parameters for automatic calculation of an assembly diagram without relaxation or temporal averaging.

3.1.2 Classification of observed phases.

To obtain an assembly diagram, we analyze each final simulation snapshot in direct space by inspection of the particle configuration as well as in reciprocal space via calculation of its diffraction pattern. The latter is important because approximants can exhibit significant phason fluctuations (see discussion below). We manually compare snapshots to tiling structures with the following wallpaper groups: $p3m1$ (2/1 approximant), $p6m$
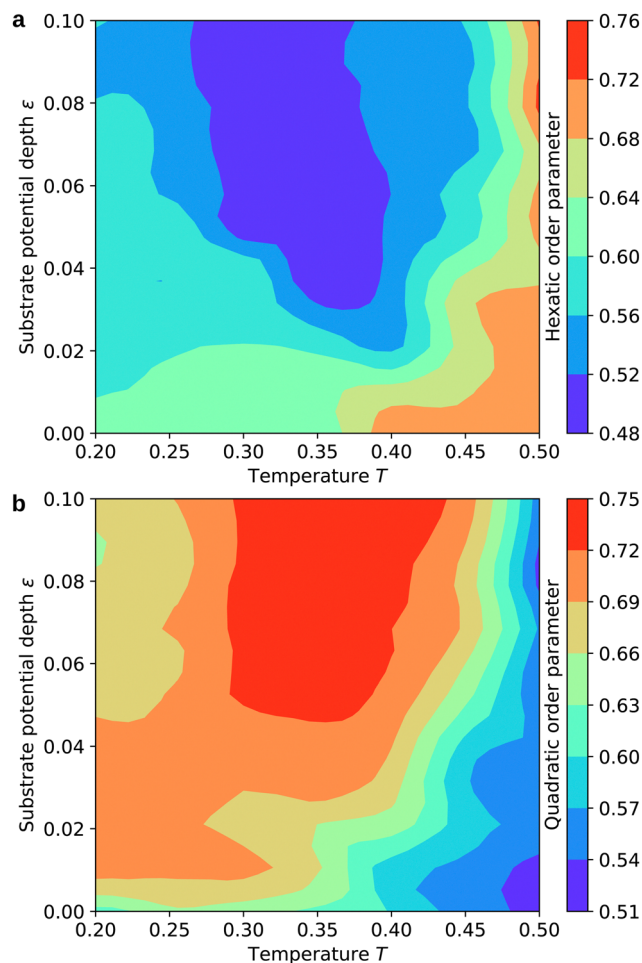

Fig. 4 Prevalence of local orientational order in final simulation snapshots of long MD simulations. Data is smoothed by cubic interpolation. (a) Hexatic order parameter Ψ_6. (b) Quadratic order parameter Ψ_4.

(other hexagonal q/p approximants), $p12m$ (dodecagonal QC), $p4m$ (square lattice), and $E(2)$ (liquid). Manual classification is typically unique and unambiguous. In the presence of multiple tiling structures or in case defects remain in simulation snapshots, a snapshot is classified as belonging to the dominant tiling structure.

We summarize the structure classification in the assembly diagram of Fig. 5. In the absence of a substrate, $\varepsilon = 0$, the known phase behavior of eqn (2) is reproduced. Notice that due to low resolution along the temperature axis, the continuous series of q/p approximants reported previously[41] is not fully resolved. Phase boundaries shift with ε according to four trends. First, the dodecagonal QC and the 3/2 approximant become stable over broader temperature ranges and shift towards lower temperatures. This finding demonstrates that a hexagonal substrate can, in fact, stabilize a dodecagonal quasicrystal despite it having lower symmetry than the quasicrystal. Second, the stability region of the square lattice shifts towards high T with an increase of ε, and a new structure, called the modulated square lattice (msq), appears. Third, melting temperature increases with ε. Fourth, at low T and high ε we find a novel
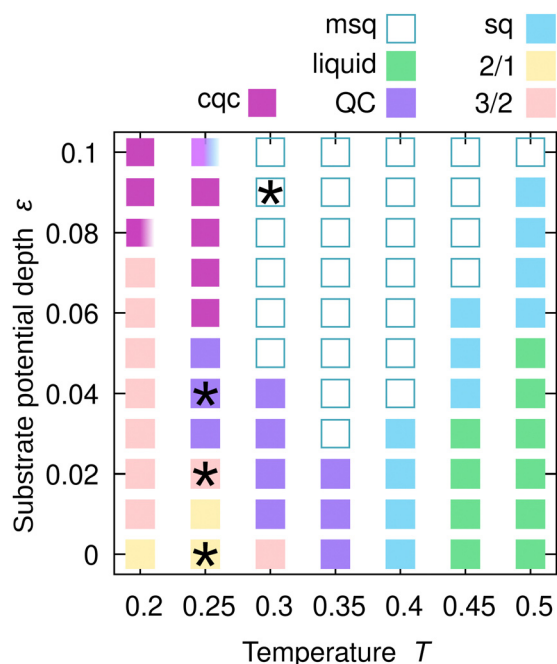
Fig. 5 Assembly diagram of the LJG potential in the T–ε parameter plane. Each data point corresponds to the dominant structure observed in the final simulation snapshot after long relaxation. The ordered structures are modulated square lattice (msq), square lattice (sq), 2/1 approximant (2/1), 3/2 approximant (3/2), dodecagonal QC (QC), and chiral structure (cqc). Snapshots at the parameter position indicated by four asterisks are shown in Fig. 6 and 8.

chiral quasicrystal (cqc). In cqc, the inversion symmetry of the dodecagonal quasicrystal is broken. Because this manuscript focuses on weak substrate potentials, cqc will be the subject of follow-up work. Three simulation snapshots at parameters marked by asterisks in Fig. 5, the 2/1 approximant at $(T,\varepsilon) = (0.25, 0.00)$, the 3/2 approximant at $(0.25, 0.02)$, and the quasicrystal at $(0.25, 0.04)$ are shown in Fig. 6. A fourth simulation snapshot at parameters marked by an asterisk at $(0.3, 0.09)$ corresponding to msq is shown in Fig. 8.

We make two further observations: first, in the absence of a substrate, the phase transformation from the 2/1 approximant to the QC was continuous *via* a series of q/p approximants. This continuous behavior is not sustained towards finite ε. Instead, higher-order approximants are generally suppressed. Specifically, we identify the low-order approximants 2/1 and 3/2 repeatedly in our snapshots for $\varepsilon > 0$ but no other approximants. Second, there remain significant phason mode fluctuations in the 3/2 approximant at elevated temperatures. Such phason mode fluctuations are apparent when comparing Fig. 6(b)-left, which shows a simulation snapshot, to Fig. 6(b)-right, which shows the ideal tiling of the 3/2 approximant obtained after slow relaxation to $T = 0$ to remove phason fluctuations. Notice the similarity of the diffraction patterns calculated for both snapshots (two halves in Fig. 6(b)-middle). Apparently, the 3/2 approximant behaves like a random tiling in that it permits phason mode fluctuations in thermodynamic equilibrium. This means we must rely on characterization of

average crystallographic order by identification of diffraction spots in the diffraction pattern to distinguish the approximants in the generation of the assembly diagram.

The presence of phason mode fluctuations in an approximant is unexpected and to the best of our knowledge has not been reported. It is unclear whether such behavior is related to the dimensionality of our system and can also occur in three dimensions. We observe random tiling behavior only in sufficiently complex approximants. For example, in the 2/1 approximant, there are no square tiles (green squares in Fig. 6) except if connected to structural defects. This means phason flips cannot occur inside a 2/1 approximant but must be initiated from the surface or from a grain boundary. In contrast, the 3/2 approximant has many square tiles and thus readily supports phason mode fluctuations.

3.2 Incommensurate–commensurate transition

While the unperturbed (*i.e.*, in the absence of a substrate) 2/1 approximant transforms into the dodecagonal QC continuously *via* a series of hexagonal approximants, all approximants except 2/1 and 3/2 quickly disappear when the substrate is turned on (Fig. 5). Why is this the case? To understand the disappearance of higher-order approximants, we resort to free energy calculations. We calculate free energies for a well-relaxed QC and a number of low-order approximants. Recall that hexagonal approximants are labeled by two integers as q/p with $(\sqrt{3}+1)/2 \approx 1.37 < q/p < 2$. Without loss of generality, we can require q and p to be coprime. Finally, q and p should be small such that the approximants have small unit cells. The simplest such approximants are 2/1 = 2, 9/5 = 1.8, 5/3 ≈ 1.67, 3/2 = 1.5, and 7/5 = 1.4. We arrange the approximants in decreasing order of the q/p ratio from the 2/1 approximant, which is the energetic ground state, to the QC, which is the equilibrium state at intermediate temperature.

Fig. 7 depicts the phase diagram predicted by free energy calculations. In the absence of a substrate, $\varepsilon = 0$, the phase diagram cycles through the approximants 2/1, 9/5, 5/3, 3/2, 7/5, and QC in correct (that is, in q/p decreasing) order with temperature. We also confirm the disappearance of all approximants except 2/1 and 3/2 with increasing ε. Note that we did not include in the free energy calculations the square lattice and its modulation and the liquid. Besides this omission, there is good agreement of the phase diagram in Fig. 7 with the assembly diagram obtained from MD in Fig. 5.

Situations where the competition of two length scales dominates phase behavior have long been studied in the field of modulated crystals.[52] Because the two length scales are of different physical or chemical origins, their ratio is not expected to be any special number and typically will be irrational. The requirement of the system to satisfy both length scales simultaneously then causes the emergence of structural complexity in the form of modulated crystals. One distinguishes two cases: incommensurately modulated crystals are aperiodic crystals where both length scales are realized without compromise. The dodecagonal QC in our system can be interpreted as an
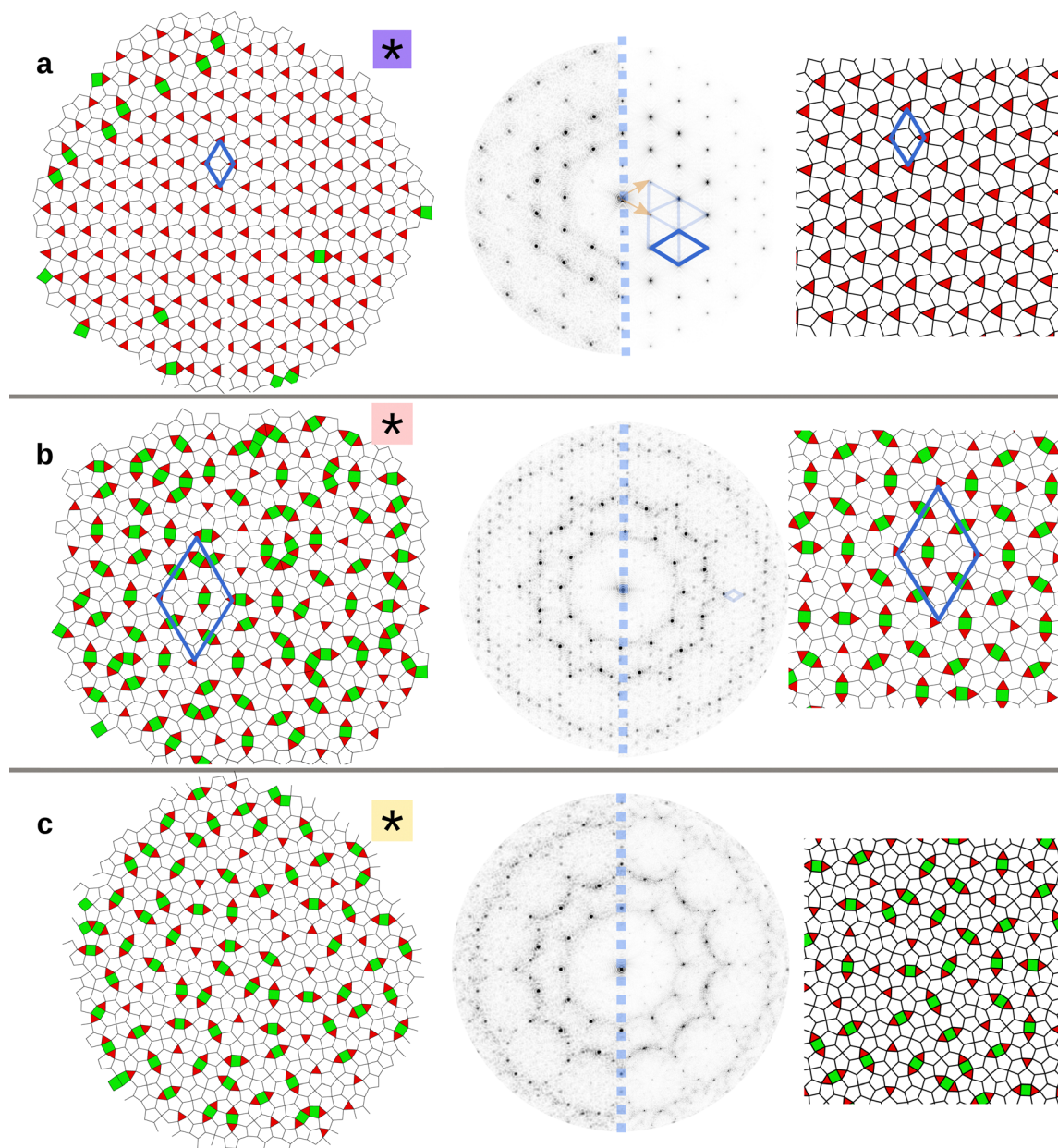
Fig. 6 Snapshots from MD simulations at $T = 0.25$ and at three substrate potential depths ε. Nearest neighbor bonds are shown only, with the particles omitted. Triangle tiles are shown in red, square tiles in green. (a) 2/1 approximant at $\varepsilon = 0.00$. (b) 3/2 approximant at $\varepsilon = 0.02$. (c) QC at $\varepsilon = 0.04$. Snapshots are shown in direct space obtained from simulation (left column) and from representative ideal tilings (right column). Diffraction patterns (middle column) are calculated and compared for both snapshots (left and right halves). The reciprocal lattice of diffraction spots in reciprocal space is mapped onto characteristic lattice vectors in direct space as indicated by blue lines in (a) and (b). Notice the presence of significant phason mode fluctuations in the simulation snapshot of the 3/2 approximant (b, left). Despite these phason mode fluctuations, its diffraction image (b, left half of middle) is highly similar to the diffraction image of the ideal tiling of the 3/2 approximant without any phason mode fluctuations (b, right half of middle).

incommensurately modulated crystal. A related example is Moiré patterns, where not a competition of length scales but the competition of crystallographic orientations and translation generates interference effects. Incommensurately modulated crystals are accompanied by phason modes in thermodynamic equilibrium. In contrast, commensurately modulated crystals are periodic crystals with large unit cells. The lattice constants of commensurately modulated crystals simultaneously approximate integer multiples of both length scales. Commensurately

modulated crystals result from a lock-in transition where the irrational ratio of the two length scales locks into a rational approximation. q/p approximants are examples of commensurately modulated crystals.

Phase diagrams that include modulated crystals are usually studied as a function of length scale ratio and coupling strength. The first parameter, the length scale ratio, is often controlled indirectly by changing the composition or local structure. In our system, the length scale ratio is linked to the
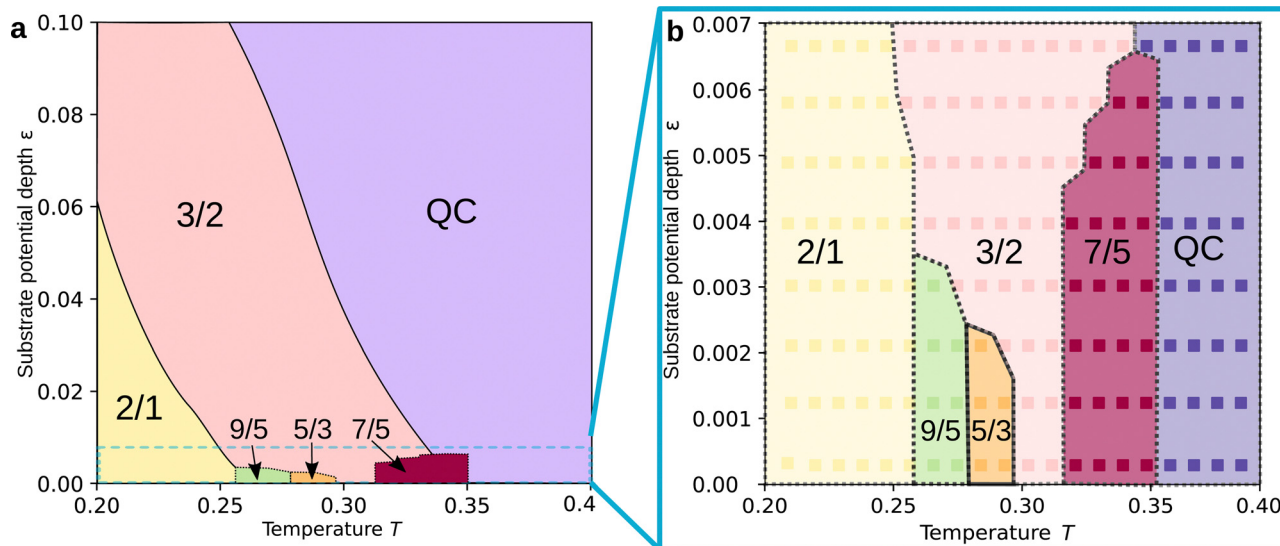
Fig. 7 (a) Phase diagram of the LJG potential with substrate from free energy calculations of the approximants 2/1, 9/5, 5/3, 3/2, 7/5, and the QC as candidates. (b) Zoom in on the region with weak substrate potential. The continuous transformation of the 2/1 approximant into the QC transitions disappears as ε increases. This phenomenon resembles the Devil's flower phenomenon known in modulated crystals where spontaneous phase-locking takes place.

temperature T because temperature affects tile energy and thus the tile type that is dominant. The second parameter, the coupling strength, is measured relative to thermal energy. In our system, the coupling strength is given by substrate potential depth ε. With these identifications, we can compare our phase diagram to past phase diagrams of modulated crystals. The comparison shows that Fig. 7 closely resembles the mean field phase diagram for the 3D Ising model with competing interactions (Fig. 24 in ref. 53) and the FVdM model as suggested by Aubry (Fig. 25 in ref. 53). Such characteristic phase diagrams of incommensurate–commensurate transitions have been called the Devils flower phenomenon by Bak.[54] Our results confirm that the increase of substrate strength locks modulated crystals into certain approximants and drives new complex phase behavior as expected from the Devil's flower phenomenon.

The appearance of the Devil's flower in our phase diagram helps us interpret the observed stabilization mechanism and particle dynamics. In the absence of a substrate in the temperature range $0.24 < T < 0.36$, the system is incommensurately modulated. Phason modes are unlocked and critical for thermodynamic stabilization because they contribute to the free energy. As substrate potential depth increases, phason modes may still be present (see Fig. 6) but gradually disappear. Eventually, the system locks into the 2/1 and 3/2 approximants. To the best of our knowledge, Fig. 7 is the first report of an incommensurate–commensurate transition in any two-dimensional system of freely moving particles.

3.3 Square lattice and its variants

The presence of the substrate drives the incommensurate–commensurate transition at low substrate potential depth $\varepsilon < 0.03$. For $\varepsilon > 0.03$, the square lattice (sq) and its variants

appear dominantly in the phase diagram (Fig. 5). For intermediate substrate potentials, a novel modulated square lattice (msq) is observed (Fig. 8(a) and (b)). For a high substrate potential, $\varepsilon \gg 1.0$, above the range covered in Fig. 5, a coexistence of grains with rectangular lattice (rec) and hexagonal lattice is eventually observed (Fig. 8(c) and (d)). All of these phenomena are yet other examples of commensurate–incommensurate transitions induced by the competition of the length scales imparted by the LJG interaction potential with the unit cell of the substrate.

Msq and rec are typically polycrystalline with individual grains locking into one of three distinct orientations. This locking is a consequence of the six-fold symmetry of the substrate. Diffraction patterns confirm the global six-fold symmetry. In the diffraction pattern of msq (inset in Fig. 8(a)), isolated peaks (circled) are present for each grain. Besides the locking of grain orientations, individual grains are only weakly affected by the substrate (see modulations discussed below). In the diffraction pattern of rec (inset in Fig. 8(c)), some peak triplets merge into single peaks (indicated by black hexagons in Fig. 8(a) and (c)). The merging is caused by a stretching of squares into rectangles to improve compatibility with the substrate. This means that the four-fold symmetry is already lost in individual grains of rec and the system is closer to six-fold symmetry than msq. While small patches of triangles are sometimes already present in rec (central part of Fig. 8(c) labelled '4'), only very high ε transforms the system completely into a hexagonal crystal (not shown).

A zoom-in on grain '2' of rec is shown in Fig. 8(d). We plot the substrate potential in the background to visualize particle locations (red) relative to maxima (yellow) and minima (green) of the potential. Potential maxima form a hexagonal
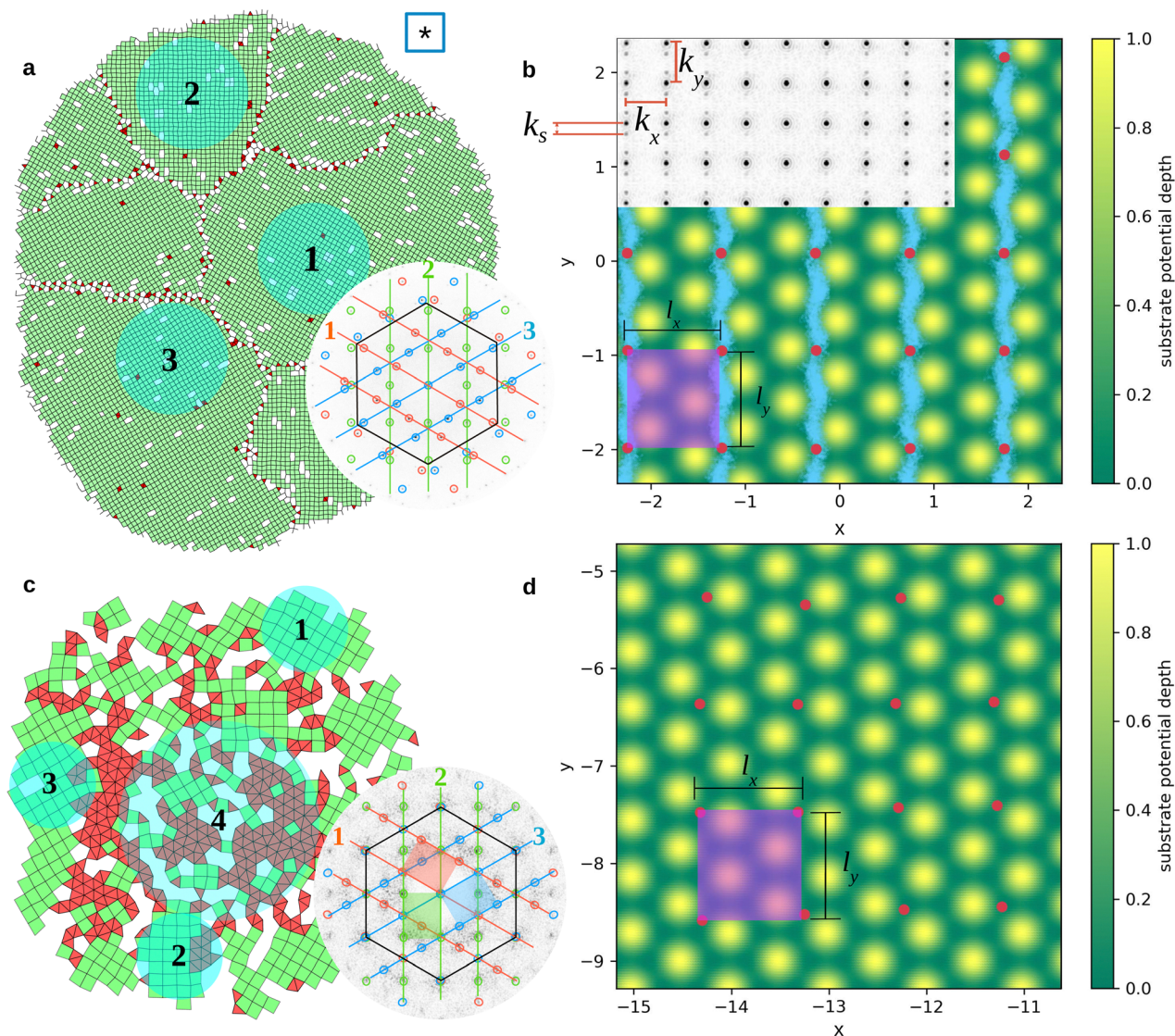
Fig. 8 Variations of the square lattice at higher substrate potential depth ε and intermediate temperature T. (a) and (b) Modulated square lattice (msq) at $\varepsilon = 0.039$ and $T = 0.3$ for 10 000 particles. (c) and (d) Coexistence of small grains with rectangular lattice (rec) and hexagonal lattice at $\varepsilon = 1.0$ and $T = 0.4$ for 1024 particles. (a) and (c) Particle configurations showing nearest neighbor bonds only, with the particles omitted. Triangle tiles are shown in red, square tiles in green. There coexist grains in three orientations (labelled '1', '2', '3') and a region dominated by triangles (labelled '4' in (d)). Diffraction patterns are shown as bottom right insets with diffraction peaks encircled and colored according to the grain orientation they correspond to. (b) and (d) Zoom ins on the grain '2'. Particles are shown as small red disks overlaid on the substrate potential. In (b) light blue color indicates the channels the particles move in. A diffraction pattern is shown as the top left inset.

lattice separated by channels of low potential that trace the nearest–neighbor bond network of a honeycomb lattice. The stretching of squares into rectangles can now be understood. Recall that the nearest–neighbor distance is $r_{\mathrm{NN}} \approx 1.0$, and the substrate periodicity is chosen as $\lambda = 0.5$. A lattice constant $l_x = 2\lambda$ allows particles to retain their preferred nearest–neighbor distance without penalty. And a slight adjustment of the lattice constant to $l_y = \sqrt{4/3}\, l_x \approx 1.15 l_x$ ensures commensurability with the substrate also in the y-direction.

A zoom-in on grain '2' of msq is shown in Fig. 8(b). Just like before, a lattice constant $l_x = 2\lambda$ allows particles to retain their preferred nearest–neighbor distance without penalty. The y-direction

is again more complicated. A lattice constant $l_y = l_x$ now guarantees four-fold symmetry in the diffraction pattern but can do so only on average and by allowing positional modulations along the y-axis. A close inspection reveals the presence of this modulation in the form of weak satellite peaks in the diffraction pattern (inset in Fig. 8(b)). The separation of satellite peaks from the central peaks corresponds to a superstructure periodicity of $l_s \approx 0.20$. Analysis of other snapshots suggests that l_s is not unique but is a function of T and ε. We also observe that particles are unusually mobile in channels along the y-direction (purple in Fig. 8(b)). This high mobility can be directly associated with a phason mode. All evidence combined demonstrates that msq is an incommensurately modulated crystal.

4 Conclusions

Research in this paper was originally motivated by the discovery of approximants in the thin-film perovskites (Ba, Sc)TiO$_3$ on solid metal substrates. Importantly, experiments demonstrated that the type of approximant changes as a function of substrate interaction and periodicity. Our findings reproduce and explain aspects of these experimental observations. Our findings also highlight a number of new phenomena, not yet seen in experiments or simulations.

The new phenomena we observed and that we believe could be general consequences of the competition between a QC and a periodic substrate, are as follows:

1. Existence of incommensurate–commensurate phase transitions. In these phase transitions, the QC locks into one or several approximants. We observed the stabilization of the 3/2 approximant *via* a lock-in transition.

2. Approximants with phason fluctuations. We observed that the 3/2 approximant resembles a random tiling rather than an ideal crystal despite having a well-defined periodicity as indicated by the presence of a reciprocal lattice.

3. Enhanced stability of the QC. Counter-intuitively, the substrate enhanced the thermodynamic stability of the dodecagonal quasicrystal for some parameter values.

4. Incommensurately modulated crystals, where the modulation is a consequence of competition between two length scales. We observed the modulated square lattice.

5. Novel structures commensurate with the substrate that are not approximants. We observed the rectangular lattice.

While observation 1 is similar to that in thin-film perovskites and observation 3 could explain the existence of perovskite QCs, the other observations have not yet been reported in the experimental system. It will be interesting to search for them.

Generally, we see a trend that the competition between the inherent symmetry of the model system, *i.e.*, the crystal structure that the system prefers to form in the absence of a substrate, and the imposed symmetry of the substrate can occur in multiple steps involving both commensurate and incommensurate phases. We find in our system, as we increase the strength of the substrate potential, at $T = 0.25$ (see Fig. 5), a complex sequence of phase transformation alternating between commensurate and incommensurate: from (i) 2/1 approximant (crystal) to (ii) 3/2 approximant (commensurate) to (iii) quasi-crystal (incommensurate) to (iv) modulated square lattice (incommensurate) to (v) rectangle lattice (commensurate) to (vi) hexagonal lattice (substrate).

Future work should further expand this research by testing more parameters or conducting similar studies in more realistic systems. An important parameter that should be varied, but was not in this work, is the substrate periodicity. Varying this parameter, it should be possible to target desired crystal structures and approximants by inverse design. Given that many recent model systems of quasicrystals have been found in soft matter systems and the fact that such systems are highly tunable and thus ideally suited for parameter studies, we believe that soft matter quasicrystals are ideal candidates to test many of the discoveries reported in this work.

Author contributions

N. R. V.-R. implemented the model and performed all simulations and free energy calculations. Both authors conceived the idea, discussed the results, and wrote the manuscript. M. E. developed code to construct tilings and supervised the project.

Conflicts of interest

There are no conflicts to declare.

Acknowledgements

Notes and references

1 D. Shechtman, I. Blech, D. Gratias and J. W. Cahn, *Phys. Rev. Lett.*, 1984, **53**, 1951–1953.
2 D. Levine and P. J. Steinhardt, *Phys. Rev. Lett.*, 1984, **53**, 2477–2480.
3 W. Steurer, *Acta Crystallogr., Sect. A: Found. Adv.*, 2018, **74**, 1–11.
4 C. Janot, *Phys. Rev. B: Condens. Matter Mater. Phys.*, 1996, **53**, 181–191.
5 S. Takeuchi, H. Iwanaga and T. Shibuya, *Jpn. J. Appl. Phys.*, 1991, **30**, 561.
6 D. S. Shatura and A. A. Enaleeva, *Crystallogr. Rep.*, 2007, **52**, 945–952.
7 Z. V. Vardeny, A. Nahata and A. Agrawal, *Nat. Photonics*, 2013, **7**, 177–187.
8 K. Kamiya, T. Takeuchi, N. Kabeya, N. Wada, T. Ishimasa, A. Ochiai, K. Deguchi, K. Imura and N. K. Sato, *Nat. Commun.*, 2018, **9**, 154.
9 S. Förster, K. Meinel, R. Hammer, M. Trautmann and W. Widdra, *Nature*, 2013, **502**, 215–218.
10 S. Förster, M. Trautmann, S. Roy, W. A. Adeagbo, E. M. Zollner, R. Hammer, F. O. Schumann, K. Meinel, S. K. Nayak, K. Mohseni, W. Hergert, H. L. Meyerheim and W. Widdra, *Phys. Rev. Lett.*, 2016, **117**, 095501.
11 S. Foerster, J. I. Flege, J. Falta, E. M. Zollner, F. O. Schumann, R. Hammer, A. Bayat, K.-M. Schindler and W. Widdra, *Ann. Phys.*, 2017, **529**, 1–7.
12 S. Förster, S. Schenk, E. Maria Zollner, O. Krahn, C.-T. Chiang, F. O. Schumann, A. Bayat, K.-M. Schindler, M. Trautmann, R. Hammer, K. Meinel, W. A. Adeagbo, W. Hergert, J. Ingo Flege, J. Falta, M. Ellguth, C. Tusche,

M. DeBoissieu, M. Muntwiler, T. Greber and W. Widdra, *Phys. Status Solidi B*, 2020, **257**, 1900624.

13 M. Maniraj, L. V. Tran, O. Krahn, S. Schenk, W. Widdra and S. Förster, *Phys. Rev. Mater.*, 2021, **5**, 084006.

14 E. M. Zollner, S. Schenk, M. Setvin and S. Förster, *Phys. Status Solidi B*, 2020, **257**, 1900620.

15 E. Maria Zollner, F. Schuster, K. Meinel, P. Stötzner, S. Schenk, B. Allner, S. Förster and W. Widdra, *Phys. Status Solidi B*, 2020, **257**, 1900655.

16 E. Cockayne, M. Mihalkovič and C. L. Henley, *Phys. Rev. B*, 2016, **93**, 020101.

17 T. T. Dorini, F. Brix, C. Chatelier, A. Kokalj and E. Gaudry, *Nanoscale*, 2021, **13**, 10771–10779.

18 A. Patrykiejew, W. Rżysko and S. Sokołowski, *Adsorption*, 2009, **15**, 254–263.

19 T. Neuhaus, M. Marechal, M. Schmiedeberg and H. Löwen, *Phys. Rev. Lett.*, 2013, **110**, 118301.

20 T. Brazda, A. Silva, N. Manini, A. Vanossi, R. Guerra, E. Tosatti and C. Bechinger, *Phys. Rev. X*, 2018, **8**, 011050.

21 M. Z. Baykara, M. R. Vazirisereshk and A. Martini, *Appl. Phys. Rev.*, 2018, **5**, 041102.

22 S. Amiri, C. A. Volkert and R. L. C. Vink, *Phys. Rev. E*, 2021, **104**, 014802.

23 X. Cao, E. Panizon, A. Vanossi, N. Manini, E. Tosatti and C. Bechinger, *Phys. Rev. E*, 2021, **103**, 012606.

24 C. Reichhardt and C. J. O. Reichhardt, *Rep. Prog. Phys.*, 2016, **80**, 026501.

25 T. Flückiger, Y. Weisskopf, M. Erbudak, R. Lüscher and A. R. Kortan, *Nano Lett.*, 2003, **3**, 1717–1721.

26 N. Ferralis, R. D. Diehl, K. Pussi, M. Lindroos, I. Fisher and C. J. Jenks, *Phys. Rev. B: Condens. Matter Mater. Phys.*, 2004, **69**, 075410.

27 B. Bilki, M. Erbudak, M. Mungan and Y. Weisskopf, *Phys. Rev. B: Condens. Matter Mater. Phys.*, 2007, **75**, 045437.

28 J. A. Smerdon, K. M. Young, M. Lowe, S. S. Hars, T. P. Yadav, D. Hesp, V. R. Dhanak, A. P. Tsai, H. R. Sharma and R. McGrath, *Nano Lett.*, 2014, **14**, 1184–1189.

29 J. Mikhael, J. Roth, L. Helden and C. Bechinger, *Nature*, 2008, **454**, 501–504.

30 M. Schmiedeberg and H. Stark, *Phys. Rev. Lett.*, 2008, **101**, 218302.

31 M. Schmiedeberg, J. Mikhael, S. Rausch, J. Roth, L. Helden, C. Bechinger and H. Stark, *Eur. Phys. J. E*, 2010, **32**, 25–34.

32 J. Mikhael, G. Gera, T. Bohlein and C. Bechinger, *Soft Matter*, 2011, **7**, 1352–1357.

33 A. Jagannathan and M. Duneau, *Eur. Phys. J. B*, 2014, **87**, 149.

34 P. W. Leung, C. L. Henley and G. V. Chester, *Phys. Rev. B: Condens. Matter Mater. Phys.*, 1989, **39**, 446–458.

35 E. Fayen, M. Impéror-Clerc, L. Filion, G. Foffi and F. Smallenburg, *Soft Matter*, 2023, **19**, 2654–2663.

36 A. Quandt and M. P. Teter, *Phys. Rev. B: Condens. Matter Mater. Phys.*, 1999, **59**, 8586–8592.

37 M. Engel and H.-R. Trebin, *Phys. Rev. Lett.*, 2007, **98**, 225505.

38 M. Engel, M. Umezaki, H.-R. Trebin and T. Odagaki, *Phys. Rev. B: Condens. Matter Mater. Phys.*, 2010, **82**, 134206.

39 M. N. van der Linden, J. P. K. Doye and A. A. Louis, *J. Chem. Phys.*, 2012, **136**, 054904.

40 A. Reinhardt, F. Romano and J. P. K. Doye, *Phys. Rev. Lett.*, 2013, **110**, 255503.

41 M. Engel, *Phys. Rev. Lett.*, 2011, **106**, 095504.

42 M. Oxborrow and C. L. Henley, *Phys. Rev. B: Condens. Matter Mater. Phys.*, 1993, **48**, 6966–6998.

43 N. de Bruijn, *Indag. Math.*, 1981, **84**, 39–52.

44 N. de Bruijn, *Indag. Math.*, 1981, **84**, 53–66.

45 F. Gähler, *Quasicryst. Mater., Proc.*, 1988, 272–284.

46 A. Kiselev, M. Engel and H.-R. Trebin, *Phys. Rev. Lett.*, 2012, **109**, 225502.

47 J. Glaser, T. D. Nguyen, J. A. Anderson, P. Lui, F. Spiga, J. A. Millan, D. C. Morse and S. C. Glotzer, *Comput. Phys. Commun.*, 2015, **192**, 97–107.

48 J. A. Anderson, C. D. Lorenz and A. Travesset, *J. Comput. Phys.*, 2008, **227**, 5342–5359.

49 D. Frenkel and A. J. C. Ladd, *J. Chem. Phys.*, 1984, **81**, 3188–3193.

50 R. K. R. Addula, S. K. Veesam and S. N. Punnathanam, *Mol. Simul.*, 2021, **47**, 824–830.

51 N. D. Mermin, *Phys. Rev.*, 1968, **176**, 250–254.

52 S. van Smaalen, *Incommensurate Crystallography (International Union of Crystallography Monographs on Crystallography)*, Oxford University Press, Oxford, 2007.

53 P. Bak, *Rep. Prog. Phys.*, 1982, **45**, 587.

54 P. Bak, *Phys. Today*, 1986, **39**, 38–45.